18th Australasian Fluid Mechanics Conference
Launceston, Australia
3-7 December 2012

High speed imaging of spherical shock standoff in hypervelocity flows

F. Zander[1], P. A. Jacobs[1], U. A. Sheikh[1] and R. G. Morgan[1]

[1]Department of Mechanical and Mining Engineering
University Queensland, Queensland 4067, Australia

Abstract

Shock standoff distance on blunt bodies is a parameter that is often used for the validation of compressible flow CFD solvers, but there is limited experimental data found in the literature for shock standoff in hypersonic flow above approximately 6.4 km/s. The objective of this work is to extend the experimental data range to include flow speeds of up to 9.6 km/s. One of the difficulties previously encountered is in accurately measuring the shock standoff. In this work the flows were imaged using a *Hypervision HPV-1* high speed camera capable of frame rates up to 1 MHz, however, during the test time the stagnation point of the model is no longer clear due to the radiating flow and the location must be estimated using the geometric matching. To fix this limitation, and to improve the resolution of the data, the images are processed using shape detection algorithms to analyse the shock standoff during the test flow.

Introduction

Computational modelling of hypervelocity flows is critical in the design of re-entry vehicles and validated simulation codes are required to meet this need. Bertin and Cummings [1] and Gnoffo et al. [2] discuss the requirement, and importance, of the validation of computational codes with experimental data. Because the measurement of experimental data requires either extensive ground testing or expensive flight testing computational fluid dynamics (CFD) codes are often verified against simplified baseline test cases which represent similar conditions to those which are being modelled. In the low speed flow regime there is plenty of data available for verification, however, when the speeds increase into the hypersonic regime of several km/s, the amount of reference data is greatly reduced. There is difficulty in generating suitable test flows and in accurately measuring parameters of interest.

A classic data set that has been used for many years for modelling verification is the Lobb sphere data [3]. This is a compilation of data points for flow speeds of up to 6.5 km/s over spheres. The more recent data by Nonaka [4] is limited to even lower speeds. The objective of the current work is to extend this data range into the higher hypersonic region with test speeds of up to 9.6 km/s. The test flows are generated in the X2 expansion tube at the University of Queensland.

This paper also introduces the new processing method being used to extract shock standoffs in the expansion tubes utilising a high speed camera with a frame rate of up to 1 MHz. A geometric fitting algorithm has been written to accurately measure the shock standoffs for each frame of video taken during the expansion tube test time.

Testing

X2 is a free piston driven expansion tube using, depending on the flow condition, two or three diagraphms and a nozzle generating steady hypervelocity flow for 50 – 150 µs. The flow that finally emerges into the test section is determined by the initial (fill) conditions in the major sections of the tube, which are shown in Fig. 1. The fill conditions used in the current study are shown in Table 1. Both conditions were tested extensively using a pitot rake to determine steady test times.

Table 1: X2 fill conditions

Shock Speed	8.4 km/s	9.6 km/s
Reservoir	6.85 MPa	6.85 MPa
Driver	742 mBar He 186 mBar Ar	742 mBar He 186 mBar Ar
Secondary Driver	NA	1100 mBar Air
Shock Tube	3 kPa Air	3 kPa Air
Acceleration Tube & Test Section	10 Pa Air	10 Pa Air

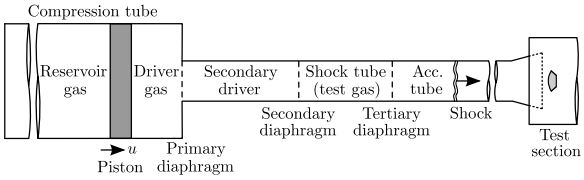

Figure 1: Physical configuration of the X2 expansion tube [5]

A total of 16 tests were undertaken in this work, 9 at the 8.4 km/s condition and 7 at the 9.6 km/s condition. Table 2 summarises the tests done showing the spherical model diameter and the shock speed of the condition. These tests are defined by the secondary shock speed which is measured in the acceleration tube prior to the nozzle. The shock speeds measured were consistent with the most extreme outliers at ±0.25 km/s of the nominal speed. The exact conditions at the model will be slightly different due to the nozzle (higher velocity, lower pressure etc.) however, for the scope of this work, the detailed condition calculation has not been included.

Table 2: Summary of sphere tests conducted

Sphere diameter	8.4 km/s	9.6 km/s
40 mm	5	2
60 mm	2	2
80 mm	2	3

The video imaging of the tests was conducted with a *Hypervision HPV-1* high speed video camera. The HPV-1 is capable of frame rates up to 1 MHz and has a CCD resolution of 316 × 260. The lens used was a Zoom Nikkor 100 – 300 mm f/5.6s lens. Figure 2 shows a schematic of the X2 test section with the HPV imaging the hemispherical model.

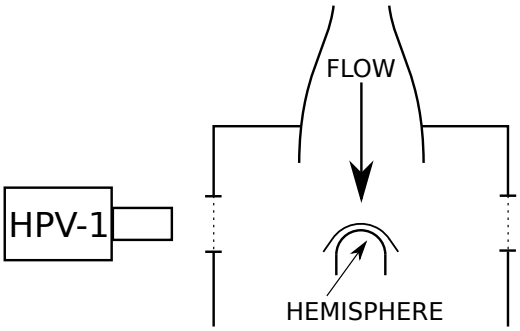

Figure 2: Optical configuration in X2

The camera settings were varied throughout the campaign with regards to frame rate and exposure time (specified as a fraction of the temporal frame spacing). This was important as the luminosity of the flow changes with speed and model size and it was important to avoid saturating the camera's sensor. Due to this iterative experimental approach some of the videos taken are under exposed, thus making the analysis difficult.

Analysis

A post processing analysis examines the high speed video recording of the tests to extract the shock standoff on the hemispheres. Individual frames are extracted from the video and used for processing. The low resolution of the camera combined with the available optics meant that the shock layer was only imaged on a small number of pixels (typically 3 – 6). This is not sufficient to accurately resolve the standoff distance and therefore a geometric fitting approach was adopted. Additionally, the fitting process is critical for accurately resolving the location of the stagnation point of the sphere, during the tests the stagnation point of the sphere is masked by the extremely hot and luminous gas making a direct measurement difficult, if not impossible.

As the models are hemispherical it is reasonable to assume that the shock in the stagnation region will form a spherical arc [6]. Assuming this, we fit circles to the model and the shock, in the stagnation region, and use these fitted circles to extract a shock standoff. The circle fitting and shock standoff measurement has been automated in *Python* utilising the additional packages *Python-numpy* and *Simple-CV*.

Starting with initial, (manually defined) 3-point estimates of the sphere and shock fitted circles, a Canny edge detection algorithm processes the image. The edge detection for the shock is limited to the near stagnation region covering a half angle of 10° – 22.5° depending on the brightness of the video being processed. This is to minimise the error associated with the hyperbolic shock shape which becomes greater with distance away from the stagnation point.

The detection of the sphere location is conducted for every image, however, there is some variability in the measured location due to either underexposure of edges or masking of exact location due to flow luminosity. This can be overcome by using the sphere location from other frames for the shock standoff measurement. Typically the videos taken include a flow startup process, the test flow and the arrival of the driver gas, and from this range of flow conditions it is usually possible to extract an accurate representation of the sphere location. This location can then be used for the time frames where the sphere's nose was obscured.

The Canny detection method returns a list of pixel locations where the shock and sphere have been detected. In order to get sub-pixel resolution on the locations, these pixel locations then have circles fitted to them using a modified least-squares fitting approach as described by Umbach [7]. This results in data with approximately an order of magnitude greater resolution than the original pixel data. The equation of a circle is given in equation 1 and the modified least squares minimisation formulation from this is shown in equation 2.

$$r^2 = (x-x_0)^2 + (y-y_0)^2 \quad (1)$$

$$SSM(x,y) = \sum_{i=1}^{n-1}\sum_{j=i+1}^{n}\left(xX_{ji} + yY_{ji} - 0.5(X_{ij}^{(2)} + Y_{ij}^{(2)})\right)^2 \quad (2)$$

The differentiation of equation 2 with regards to x and y leads to the linear equation set shown in equations 3 – 9 [7].

$$x_M = \frac{DC - BE}{AC - B^2} \quad (3)$$

$$y_M = \frac{AE - BD}{AC - B^2} \quad (4)$$

$$A = n\sum_{i=1}^{n} x_i^2 - \left(\sum_{i=1}^{n} x_i\right)^2 \quad (5)$$

$$B = n\sum_{i=1}^{n} x_i y_i - \left(\sum_{i=1}^{n} x_i\right)\left(\sum_{i=1}^{n} y_i\right) \quad (6)$$

$$C = n\sum_{i=1}^{n} y_i^2 - \left(\sum_{i=1}^{n} y_i\right)^2 \quad (7)$$

$$D = 0.5\left\{n\sum_{i=1}^{n} x_i y_i^2 - \left(\sum_{i=1}^{n} x_i\right)\left(\sum_{i=1}^{n} y_i^2\right) + n\sum_{i=1}^{n} x_i^3 - \left(\sum_{i=1}^{n} x_i\right)\left(\sum_{i=1}^{n} x_i^2\right)\right\} \quad (8)$$

$$E = 0.5\left\{n\sum_{i=1}^{n} y_i x_i^2 - \left(\sum_{i=1}^{n} y_i\right)\left(\sum_{i=1}^{n} x_i^2\right) + n\sum_{i=1}^{n} y_i^3 - \left(\sum_{i=1}^{n} y_i\right)\left(\sum_{i=1}^{n} y_i^2\right)\right\} \quad (9)$$

The radius of the calculated mean circle can then be found with Eq. (10).

$$r_M = \sum_{i=1}^{n} \frac{\sqrt{(x_i - x_M)^2 + (y_i - y_M)^2}}{n} \quad (10)$$

This equation set is solved for x_M, y_M and r_M twice for every image analysed, once for the sphere and once for the shock. The shock standoff can then be calculated

$$\Delta = (x_0 - R)_{sphere} - (x_0 - R)_{shock} \quad (11)$$

Results

Figure 3 shows an example image taken from shot x2s1684 (80 mm hemisphere, 8.4 km/s) with the fitted circles overlaid onto the image. The fitted circles are shown with comparatively thick lines for clarity, however, the computation has a much finer resolution than that shown.

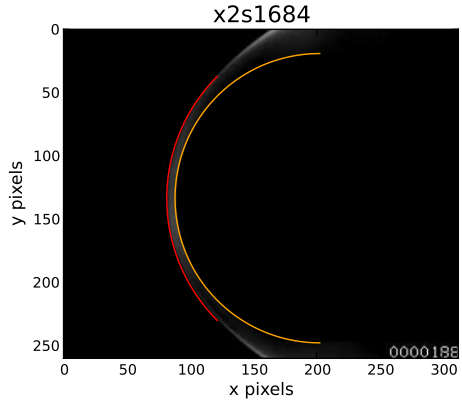

Figure 3: Example of circle fitting on sphere image

This shows that the fitted curves visually match the shock and sphere shape very well. This check is important as it is the only verification of the fitting procedure and especially in the case of the underexposed images gives confidence in the calculated standoff measurements.

Figure 4 summarises the results of all the test conducted. The experimental data is plotted using the mean of the shock standoff during the steady test time for which processable frames were available. The standoff data is normalised by the diameter of the model. The variations are specified by the minimum and maximum standoff values computed. The original Lobb data is included in the plot showing that the trend of the results is reasonable.

The shock standoff appears to be flattening out in the higher velocity regime and this is due to the thermochemistry effects which become much stronger in the higher enthalpy flows. The finite rate CFD simulation of the bluff body flows indicate a stagnation region temperature of 16600 K whereas, the ideal gas estimate of temperature (realised just after the shock) is more like 23500 K. At higher temperatures the flow enthalpy is absorbed by the chemical reactions behind the shock (disocciation, ionisation) resulting in a lower temperature, higher density flow region (in comparison with a frozen flow). Because the shock standoff is approximately proportional to the density ratio across the shock, this 'self regulation' of the density behind the shock causes the shock standoff to asymptote with velocity (or enthalpy).

The errors associated with the data are deemed to be primarily due to the camera configuration in individual tests. The videos with much lower recorded luminosity have a greater error in the measurement. For future testing, the optimal camera configurations are now known and data sets with increased accuracy can be accumulated. Since the scatter is similar to the variation seen in the original Lobb data at lower speeds, we believe that the new data sets hold value for CFD validation at the higher speeds.

Also of great interest from this work is the time evolution of the shock standoff during the expansion tube flow. Figures 5 and 6 show the evolution of the computed standoff during the test time for the two different shock speeds. This shows that there is some variation during the test time. Some data points have been filtered out where a measured variation can be directly correlated to an abberation in the video corresponding to a diagraphm particle, or other piece of debris, striking the model. The remaining variation is not (necessarily) computational error as some 'pulsing' of the flow is evident in the videos. This is an real flow variation that occurs during some, but not all, tests.

An optical feature of interest seen in the temporally resolved plots is the smoothing of data with slower frame rates. The exposure time of the images is half the frame spacing (i.e. a 4 μs/frame video has an exposure time of 2 μs) and this results in some integration of the standoff over this time. This sometimes appears to smooth out the smaller variations due to the flow effects and is particularly apparent in the 9.6 km/s data points where more of the tests were conducted using 4 μs frame times. From these images, it appears that the 9.6 km/s flow is steadier, however, from other tests with pitot pressure measurements it is known that this is not necessarily true. Further testing will concentrate on higher frame rate video capture for direct comparison purposes with the 8.4 km/s condition. There is also an argument to be made that the longer temporally-integrated images may give a fair representation of the average shock standoff.

Conclusions

This work has built the platform for, and presented preliminary results, extending the Lobb sphere shock standoff data into the higher speed ranges with flow velocities of up to, and in excess of, 9.6 km/s. An analysis method has been developed using the high speed camera and geometric fitting techniques to achieve a high resolution measurement of the shock standoff on spherical models. The preliminary results are already very useful data points and the future objectives are to extend the speed range further and to tighten the uncertainty on the experimental data.

Acknowledgements

This work is supported by the Australian Research Council Discovery Grant Scheme through grants DP1094560 and DP120102663.

References

[1] Bertin, J.J., and Cummings, R.M., Critical Hypersonic Aerothermodynamic Phenomena, *Annual Review of Fluid Mechanics*, **38**, 2006, 129–157.

[2] Gnoffo, P.A., Weilmuenster, K.J., Hamilton II, H.H, Olynick, D.R. and Venkataphathy, E., Computational Aerothermodynamic Design Issues for Hypersonic Vehicles, *Journal of Spacecraft and Rockets*, **36**, 1, 1999, 21–43.

[3] Lobb, R.K., Experimental Measurement of Shock Detachment Distance on Spheres fired in Air at Hypervelocities, in *The High Temperature Aspects of Hypersonic Flow*, editor W.C. Nelson, Pergamon Press, Oxford, 1964, 519–527.

[4] Nonaka, S., Mizuno, H., Takayama, K. and Park, C., Measurement of Shock Standoff Distance for Sphere in Ballistic Range, in *Journal of Thermophysics and Heat Transfer*, **14**, 2, 2000, 225–229.

[5] Gildfind, D.E., "Development of High Total Pressure Scramjet Flow Conditions using the X2 Expansion Tube," Ph.D. Dissertation, Centre for Hypersonics, Univeristy of Queensland, 2012 (submitted)

[6] Billig, F.S., "Shock-wave shapes around spherical-and cylindrical-nosed bodies," in *Journal of Spacecraft*, **4**, 6, 1967, 822–823.

[7] Umbach, D. and Jones, K.N., A Few Methods for Fitting Circles to Data, *IEEE Transactions on Instrumentation and Measurement*, **52**, 6, 2003, 1881–1885.

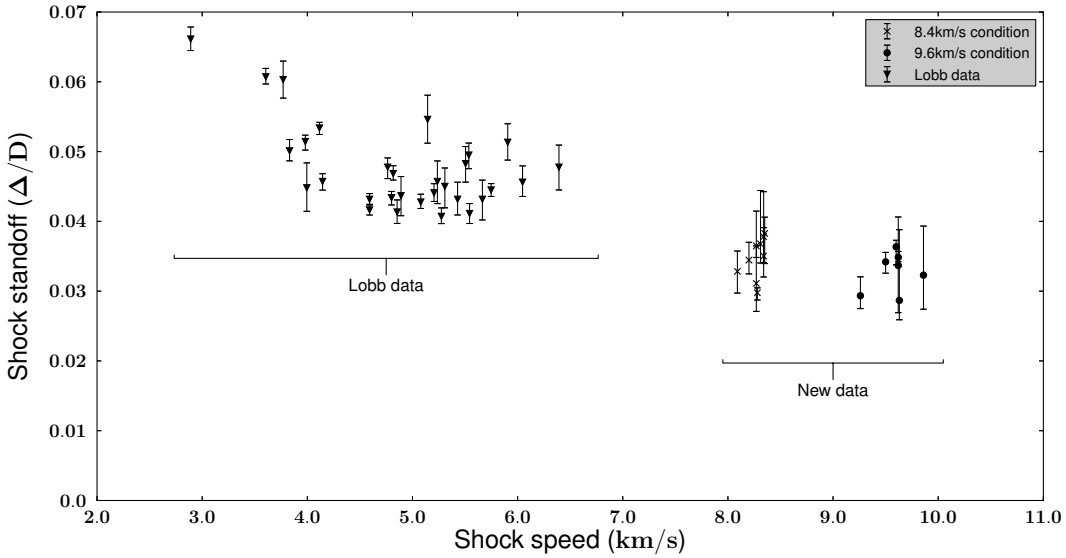

Figure 4: Experimental results with Lobb data

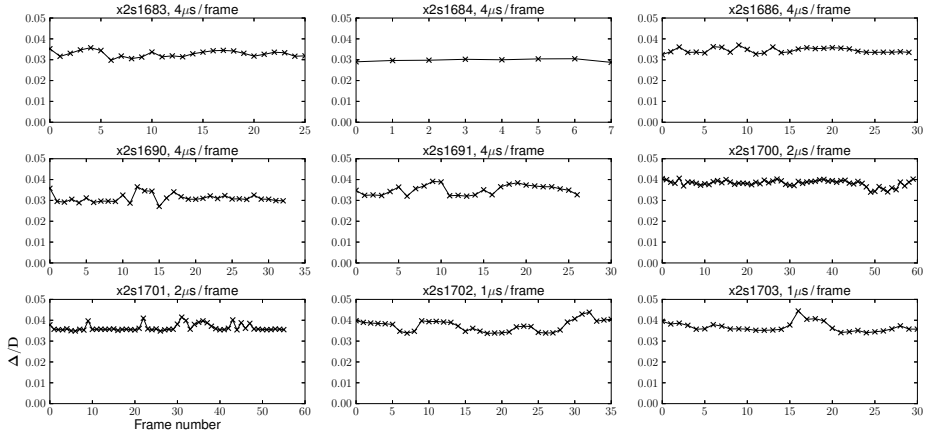

Figure 5: Time evolution of the shock standoff for the 8.4 km/s tests

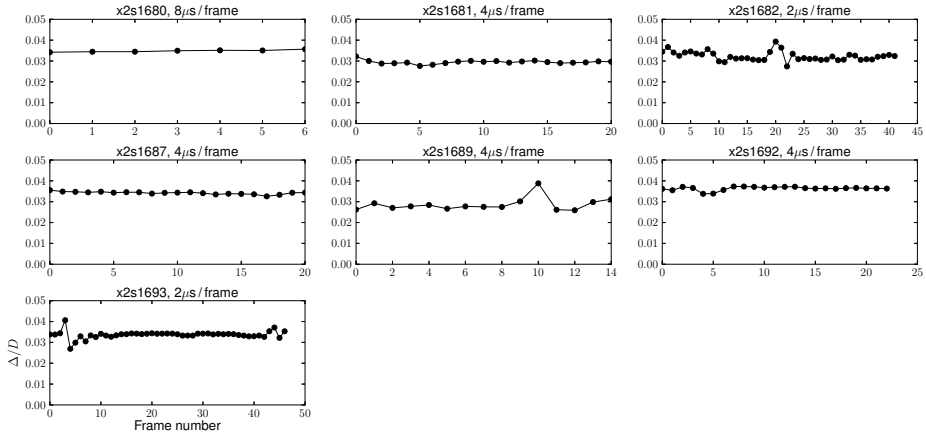

Figure 6: Time evolution of the shock standoff for the 9.6 km/s tests